

# Design of a Passive Millimeter-wave Imager Used for Concealed Weapon Detection BHU-2D-U

Bao-hua Yang<sup>1</sup>, Zhi-ping Li, Cheng Zheng, Jin Zhang, Xian-xun Yao, An-yong Hu, Jun-gang Miao  
School of Electronic and Information Engineering, Beihang University, Beijing, 100191, China  
yangbaohua728@163.com

*Abstract:* - A passive millimeter-wave imager BHU-2D-U is introduced for detecting concealed weapons on human body. It is a subsequent model of BHU-2D. The improvements of BHU-2D-U over BHU-2D are introduced. Firstly, the field of view (FOV) of the new imager is enlarged and an U type antenna of array is adopted for whole body scan. Secondly, the enlarged FOV requires smaller antenna spacing and compact receiver arrays. The I/Q demodulators operating in double side band mode is proved for no mirror-image. In order to avoid the image-reject filter between front end and IF module, this structure mode is adopted. Thirdly, the front-end circuit and IF circuit are introduced, the good consistency and the orthogonal error are obtained. Fourthly, compared with the BHU-2D, the quantity of the receiving elements is increased to 48 unites. To cope with the increase of the correlator quantity, a multiplexing technique is used in the FPGA internal layout of the correlator array unit. Finally, the design and image reconstruction algorithms are verified based on the imaging experiments on a person with concealed weapon. The initial results of BHU-2D-U have showed the effectiveness improvements.

*Key-Words:* - Concealed weapon detection, front end, passive microwave radiometry, receiver, synthetic aperture imaging

## 1 Introduction

The human security inspection has become the common focus of many governments, and its security, humanization and efficiency are raised with high requirement[1]. As millimeter wave (mmW) electronic technology develops, the passive mmW imaging technique is becoming an effective approach to detect dangerous objects under the clothes, such as concealed weapons or plastic explosive[1-3] without emitting electromagnetic energy [1-11]. Compared with the conventional X ray human security inspection system, the passive mmW system is safe for the human body. However, the image quality of these instruments is often limited by low-level signal to noise ratio (SNR) which leads to long integration time. Synthetic aperture interferometric radiometer (SAIR) is an effective technique which has the high imaging rate and large field of view (FOV) required in security applications [11-14].

Various passive MMW imaging systems have been developed by the Electromagnetic Laboratory of Beihang University[15-18]. BHU-2D-U is an improved model of BHU-2D [17], which has validated the design principle and imaging reconstruction algorithm. In order to increase the FOV to meet the requirements of whole human body scan in security applications, the main goal of

the improvements over the old model is developed. From Table I, the comparison between BHU-2D-U and BHU-2D is shown. For the BHU-2D the effective imaging area is about 1m in width and 1m in height when a person stands in front of the instrument and the distance between them is 3m, which is not enough for whole human body scan. As is shown in Fig.1, 1m in width and 2m in height are usually required, which corresponds to a rectangular FOV of  $19^\circ \times 37^\circ$ . Finally,  $22^\circ \times 40^\circ$  is used to preserve some margin for the BHU-2D-U. The different element spacings are required along the horizontal and vertical orientation because of obtaining this rectangular FOV. Then, a U-shaped array is used in the new model which is named BHU-2D-U. Since the FOV along vertical orientation is about two times larger than BHU-2D, the element spacing becomes smaller, which requires smaller receiving elements. In order to reduce the dimensions the bond-wire technology and the I/Q demodulators operating in double side band (DSB) mode are adopted.

The result of small element spacing is an increasing in correlator quantity, as shown in Table I. A multiplexing technique is used in the internal layout of the field programmable gate array (FPGA) to cope with the problem.

TABLE 1 COMPARISON BETWEEN BHU-2D-U AND BHU-2D

Parameter	BHU-2D-U	BHU-2D
Center Frequency	34.0GHz	34.1GHz
Receiver Bandwidth	400MHz	160MHz
LO Frequency	32GHz (used for RF front end)	2GHz (used for I/Q demodulator)
Field of View	22° (horizontal) 40° (vertical)	20° (circular FOV)
Synthetic Beamwidth	1.4° (horizontal) 1.2° (vertical)	1.1°
Temperature Sensitivity	~1.0K (1s integration time)	~0.7K (1s integration time)
Geometry of Antenna Array	U-shaped	Y-shaped
Number of Receiving Elements	48	24
Antenna Element Spacing	2.62 λ (horizontal) 1.46 λ (vertical)	3.07 λ
Number of Baselines	1267	427
Receiver Type	Dual conversion (DSB for I/Q demodulator)	Dual conversion (SSB for I/Q demodulator)
Number of Correlators	2704 (2676 is effective)	924
Number of Cross Correlators	2560 (2532 is effective)	852
Power Measurement System	8bit ADC and auto correlator	Statistical power measurement method [17]
Calibration	Noise Injection (External Point Source) Background Cancellation	

The system design and instrument description is discussed in Section II and III respectively. The experiment results are described in Section IV followed by conclusions.

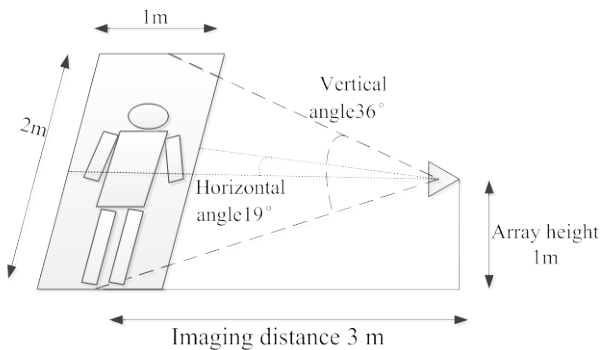


Fig.1. The imaging distance of whole human body

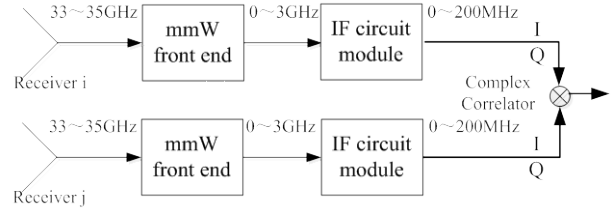


Fig.2. Block diagram of a single interferometer

## 2 System Design

### 2.1 Imaging Principle Review

The spectral components of the brightness temperature distribution in the FOV is to measured by microwave interferometry. Fig. 2 shows a block diagram of a single interferometer that is any couple of antennas in the SAIR. The visibility function or spatial frequency  $V_{ij}$  can be obtained by measuring the complex cross-correlation of the signals  $\tilde{s}_i(t)$  and  $\tilde{s}_j(t)$  collected by the pair of antennas  $i$  and  $j$ . [19]

$$\begin{aligned}
 V_{ij}(u,v) &= \frac{1}{k_B \sqrt{B_i B_j} \sqrt{G_i G_j}} \cdot \frac{1}{2} \langle \tilde{s}_i(t) \tilde{s}_j^*(t) \rangle \\
 &= \frac{1}{\sqrt{\Omega_i \Omega_j}} \iint_{\xi^2 + \eta^2 \leq 1} \frac{T_B(\xi, \eta)}{\sqrt{1 - \xi^2 - \eta^2}} \\
 &\quad \cdot F_{ni}(\xi, \eta) \cdot F_{nj}^*(\xi, \eta) \tilde{r}_{ij} \left( -\frac{u_{ij}\xi + v_{ij}\eta}{f_0} \right) \\
 &\quad \cdot e^{-j2\pi(u\xi + v\eta)} d\xi d\eta
 \end{aligned} \tag{1}$$

where  $k_B = 1.38 \times 10^{-23} \text{ J} \cdot \text{K}^{-1}$  is the Boltzmann's constant,  $(u, v)$  is the vector between the two antennas in wavelength, which is usually called baseline.  $\Omega_{i,j}$  and  $F_{ni,nj}(\xi, \eta)$  are the equivalent solid angle and normalized radiation voltage patterns of the antennas.  $B_{i,j}$  and  $G_{i,j}$  is the noise bandwidth and power gain of the receiving elements, respectively.  $\xi = \sin(\theta) \cos(\varphi)$  and  $\eta = \sin(\theta) \sin(\varphi)$  are the direction cosines in spherical coordinate system.  $f_0$  is the center

frequency of the receivers.  $T_B$  is the brightness temperature of the target.

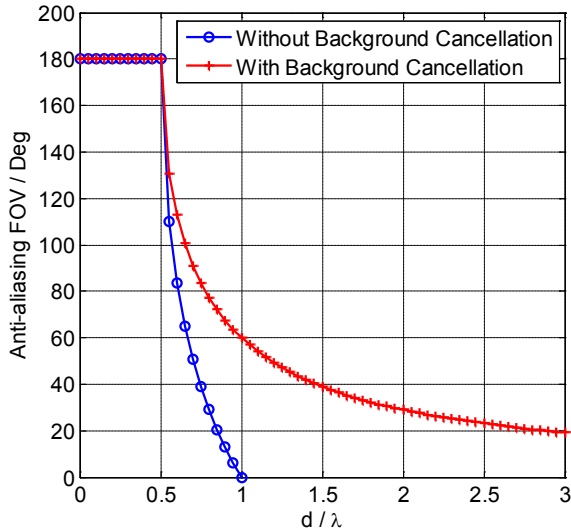


Fig.3. The anti-aliasing FOV of the SAIR with/without background cancellation

$\tilde{r}_{ij}(-\tau)$  is fringe washing function (FWF) and can be expressed as

$$r_{ij}(\tau) = \int_0^\infty H_{ni}(f) H_{nj}^*(f) e^{j2\pi f \tau} df \quad (2)$$

where  $H_{ni}(f)$  and  $H_{nj}(f)$  are the normalized frequency responses of the two receivers. Usually,  $H_{ni}(f)$  is almost the same as  $H_{nj}(f)$  and  $\tilde{r}_{ij}(-\tau)$  can be approximated by 1 [19]. Consequently,  $T_B(\xi, \eta)$  could be reconstructed by calculating the Inverse Fourier Transform (IFT) of the visibilities based on Equation (1).

Equation (1) is an integral form of the imaging principle. Corresponding to the baseline can be measured, each pair of the antennas in the array composes a baseline and the visibility function  $V(u, v)$ . Consequently, the visibility function is sampled by the antenna array. When the sampling spacing does not meet the Nyquist Theorem, aliasing error will be introduced in the

SAIR system. Generally, the anti-aliasing FOV along  $\xi$  or  $\eta$  axis could be expressed as

$$\theta_{\max} = 2 \arcsin(1/d - 1) \quad (3)$$

where  $d$  in wavelength is the spacing between visibility function samples along axis  $u$  or  $v$ . Fig. 3 shows the relationship between the sampling spacing and the anti-aliasing FOV. As can be seen,  $d < 1$  is required to guarantee an anti-aliasing FOV. On the other hand, the angular resolution in this condition could be [20]

$$\Delta\xi \approx \frac{\pi\lambda}{4\rho_{\max}} \approx 0.8 \frac{\lambda}{\rho_{\max}} \quad (4)$$

where  $\lambda$  is the wavelength corresponding to the center frequency of the receiver,  $\rho_{\max}$  is the largest baseline along  $u$  or  $v$  direction. Therefore, for a required angular resolution and FOV, Equation (3) requires a small spacing between visibility samples

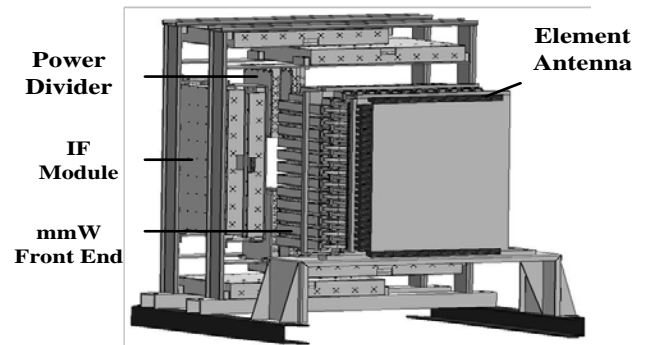


Fig.4. Antenna array of BHU-2D-U

while Equation (4) requires large coverage of the spatial frequency. For BHU-2D-U, the FOV is about  $22^\circ \times 40^\circ$  and the resolution is about  $1.4^\circ$ , which requires about 115 receiving elements and more than 10000 cross correlators. To reduce the complexity and cost of the imager, background cancellation method is used in BHU-2D-U, which is used to reduce the influence of the aliasing error caused by under sampling of the visibility function. For a given  $d$ , the anti-aliasing FOV with background cancellation is [17]

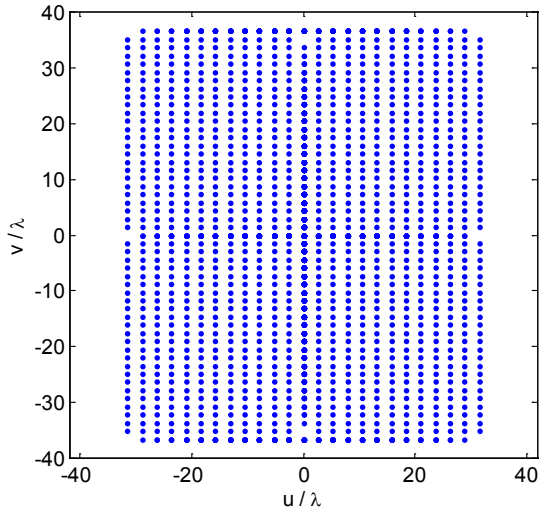


Fig.5. Distribution of visibility function samples

$$\theta_{\max}^{BC} = 2 \arcsin(1/2d) \quad (5)$$

As it is shown in Fig. 3, the anti-aliasing FOV with background cancellation is expanded for a given  $d$ . However, when background cancellation is applied, the visibility function samples need to be pre-processed before image reconstruction. The pre-processed visibility function sample is

$$V_{norm}(u,v) = \frac{V_T(u,v) - V_B(u,v)}{V_C(u,v) - V_B(u,v)} \quad (6)$$

where  $V_B(u,v)$  is the visibility of the background,  $V_T(u,v)$  is the visibility of the target and  $V_C(u,v)$  is the visibility of a calibration point source. With background cancellation method, the requirement of  $d$  is reduced. For BHU-2D-U, 48 receiving elements and 2532 cross correlators are required, which is simpler than the scheme of 115 receiving elements.

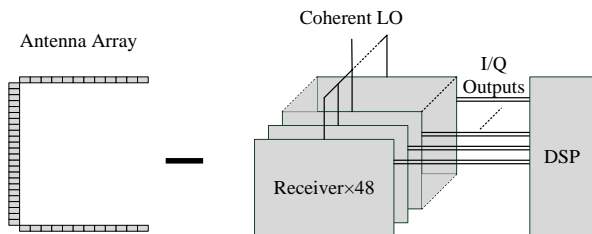


Fig.6. System configuration of BHU-2D-U

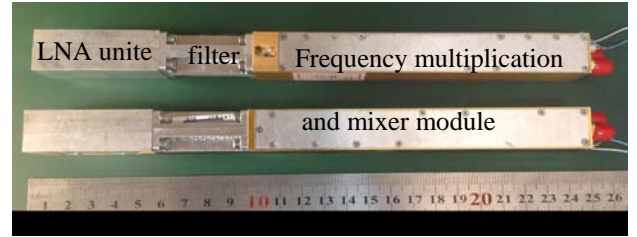


Fig.7. The mmW front end of receiving element

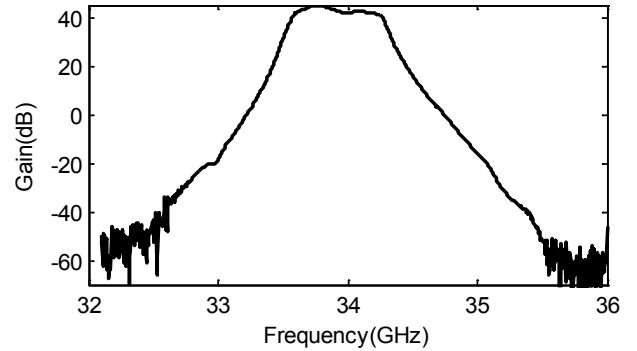


Fig.8. The measurement result of the mmW front end

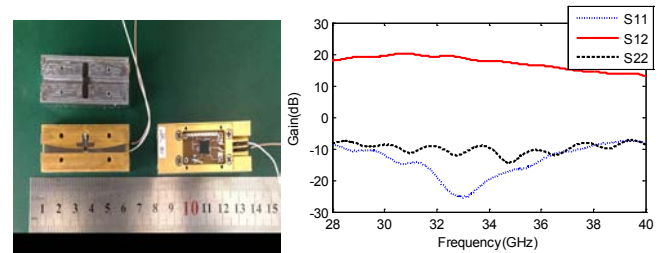


Fig.9. The LNA unite of mmW front end

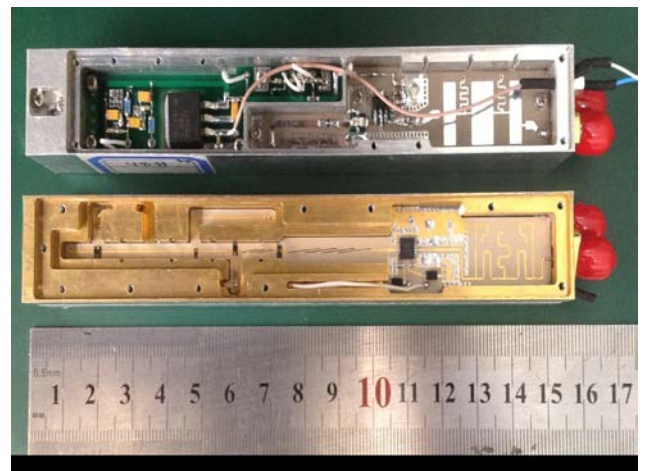


Fig.10. Frequency multiplication and mixer module of front end

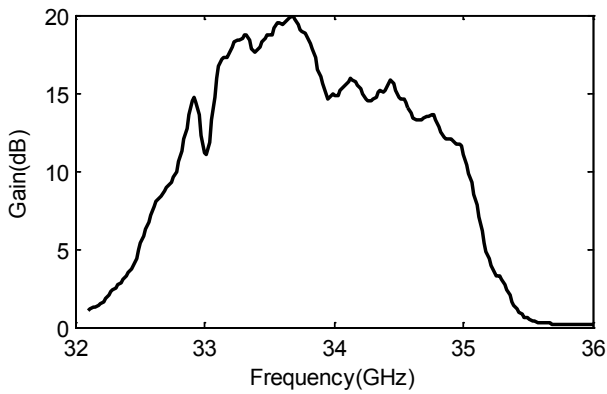


Fig.11. The measurement result of frequency multiplication and mixer module

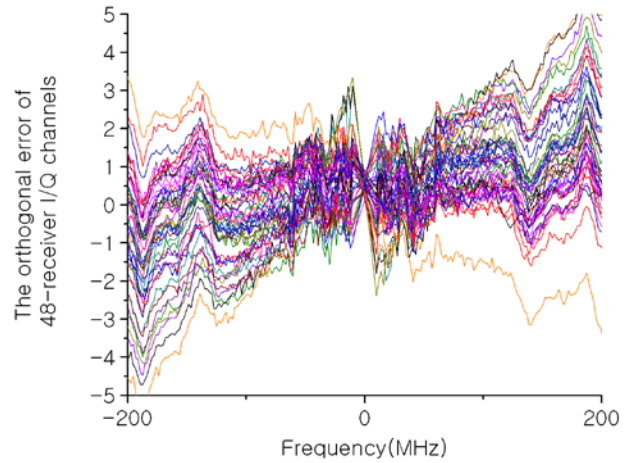


Fig.14. The The orthogonal error of 48-receiver I/Q channels

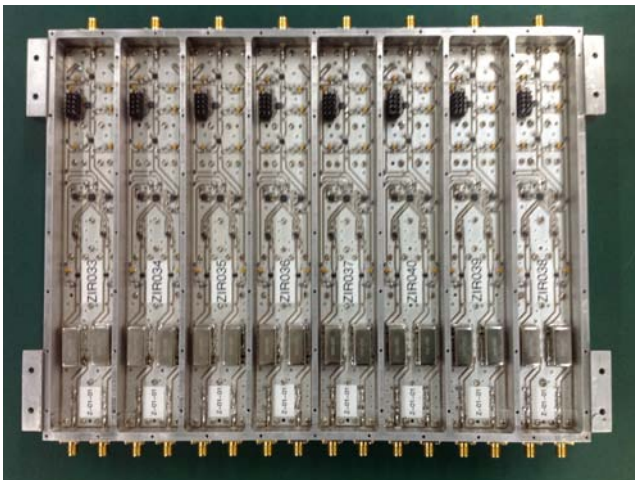


Fig.12 8 IF unites of receiving element

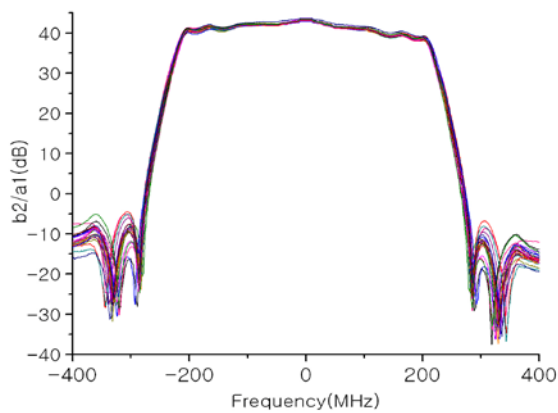


Fig.13. The measurement results of IF module

### 2.2 Antenna Array of BHU-2D-U

Based on background cancellation method, the antenna array of BHU-2D-U is designed. There are 48 receiving elements in BHU-2D-U and they are installed on a plane in U-shaped geometry. The U-shaped configuration is adopted because it can provide different visibility sample spacings along axis  $u$  and  $v$ , which leads to a rectangular FOV fitting for the application of concealed weapon detection.

Fig. 4 shows the configuration of the array. There two horizontal arms and one vertical arm. The vertical arm contains 24 receiving elements and the spacing is  $1.46 \lambda$ , while the horizontal arm contains 12 receiving elements and the spacing between elements is  $2.62 \lambda$ . The distribution of the visibility function samples are pictured in Fig. 5. There are 1267 unique baselines in the system. The largest baseline of the instrument is  $31.45 \lambda$  and  $36.55 \lambda$  along horizontal and vertical orientations, respectively, which lead to a resolution of  $1.4^\circ \times 1.2^\circ$ .

### 2.3 Structure of IF receiver

The receiver, which are I/Q demodulation after down-conversion, is adopted in the system. As see Fig.15, the first MIXER is used to realize down-conversion at single-sideband mode and then the I/Q demodulator is used at double-sideband mode.

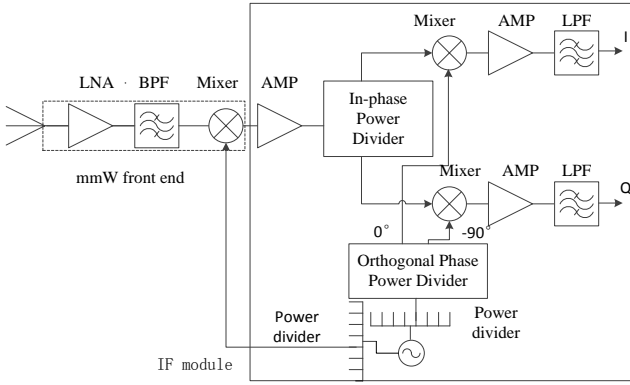


Fig 15. Configuration of one receiver

It must be considered the mirror-image when the synthetic aperture radiometer work mode is decided. The I/Q demodulation after down-conversion at single-sideband mode is analyzed, the input RF signal is represented as  $\tilde{s}_i(t)$ ,  $\tilde{s}_{LO}$  is LO signal,

$S_{IFx\_I}$  and  $S_{IFx\_Q}$  is the IF output signal of  $I$  channel and  $Q$  channel. Suppose  $m$  and  $n$  is the two random channels of the synthetic aperture radiometer, the input signal of receiver and LO can be represented respectively as[21]

$$\begin{aligned} S_{IFm\_I} &= \frac{\sqrt{2}}{4} A(t) a_{LO} \cos(2\pi f_{IF0}t + \Phi(t) - \phi_{LO}) \\ S_{IFm\_Q} &= \frac{\sqrt{2}}{4} A(t) a_{LO} \sin(2\pi f_{IF0}t + \Phi(t) - \phi_{LO}) \\ S_{IFn\_I} &= \frac{\sqrt{2}}{4} A(t) a_{LO} \cos(2\pi f_{IF0}t - 2\pi f_0\tau + \Phi(t) - \phi_{LO}) \\ S_{IFn\_I} &= \frac{\sqrt{2}}{4} A(t) a_{LO} \sin(2\pi f_{IF0}t - 2\pi f_0\tau + \Phi(t) - \phi_{LO}) \end{aligned} \quad (7)$$

Based on Equation (7), the visibility function  $V(u, v)$  of the baseline about  $m$  and  $n$  is

$$\begin{aligned} V(u, v) &= \frac{1}{2} \langle S_{IFm}(t) [S_{IFn}(t)]^* \rangle \\ &= \frac{a_{LO}^2}{16} \langle [A(t)]^2 \rangle e^{-j2\pi(u\xi_0 - v\eta_0)} \\ &= F^1 [2P\delta(\xi - \xi_0, \eta - \eta_0)] \end{aligned} \quad (8)$$

Where the  $A(t)$  and  $\Phi(t)$  are the envelope and phase of signal, the bandwidth is decided by them, the  $f_0$  is center frequency,  $\tau$  is the time difference between the radiant source and the two channels,

$$\tau = \frac{u\xi_0 - v\eta_0}{f_0}, (u, v) \text{ is the base line of the two}$$

channels,  $(\xi_0, \eta_0)$  is the cosine function of the radiant source coordination. If  $f_{LO} < f_0$  and  $f_{IF0} = f_0 - f_{LO}$ ,  $f_{IF0}$  is the IF output signal.

As can be seen in Equation (8), the brightness temperature of the radiant  $(\xi_0, \eta_0)$  could be get simply, after Fourier conversion. There are not mirror-image by adopting the I/Q demodulation after down-conversion. As a brief, this receiver structure is adopted because it does not need the image-reject filter before IF module, which is usually a bulky one.

The  $A_{mI}$  equals to  $A_{mQ}$  ideally, and the phase difference of I and Q channels is  $90^\circ$  ideally. So the phase information of the input RF signal can be get from the following formula

$$\frac{S_{IFm\_Q}}{S_{IFm\_I}} = \text{tg}(2\pi f_{IF0}t + \Phi(t) - \phi_{LO}) \quad (9)$$

The the phase information of the input RF signal  $(\Phi(t) - \phi_{LO})$  can be get from Equation (9).

Therefore, the good consistency is needed by  $A_{mI}$  and  $A_{mQ}$  that is the power of the output signals of the I/Q channels, the orthogonal phase is needed by the phase difference of the output signals of the I/Q channels.

### 3 Instrument Description

#### 3.1 System Configuration

A block diagram of BHU-2D-U is showed in Fig. 6. The instrument consists of 48 receiving elements located in a U-shaped geometry. Each element is composed of a pyramid horn and a dual-conversion receiver with I/Q demodulator. Coherent LOs are generated by a frequency synthesizer and fed into receivers through a group of dividers. Digital Signal Processing subsystem (DSP) computes the cross-correlations between the IF output signals of all receivers simultaneously and reconstruct the brightness temperature image.

### 3.2 Receiving Elements

Each receiving element in the antenna array is composed of an element antenna and a dual-conversion receiver. Fig. 7 shows the component of the receiving element.

In order to cover the rectangular and wide FOV, a pyramid horn is used as the element antenna for its simplification. The outer dimension of the horn is  $2.62\lambda \times 1.46\lambda$ , which can make full use of the spacing between antennas and maximize the main beam efficiency. The -3dB beam-width of the antenna is about  $28^\circ \times 36^\circ$ , which could be accepted for the requirements of  $19^\circ \times 37^\circ$ .

The signals collected by the antennas are fed into a group of dual-conversion receivers with I/Q demodulators. As it is shown in Fig. 2, each receiver consists of a mmW front end and an IF module, and from Fig 7 the mmW front end is composed by LNA unite, waveguide filter, and frequency multiplication and mixer module. The waveguide filter is used for the single side of the first frequency down conversion and the suppression of the imaging frequency 30GHz. The frequency response of one mmW front end is illustrated in Fig 8. It shows that the center frequency is 34 GHz and the bandwidth is 500 MHz. From Fig 9 it shows that the LNA unite is manufactured with fin line in waveguide box and the LNA chip is linked by bond wire and its measurement result is illustrated whose input and output return loss is -12 dB and -22 dB respectively after matching and its gain is 19 dB. The frequency multiplication and mixer module of front end and its DC supply can be seen in Fig 10 and its frequency response can be seen in Fig 11. Its gain is near 16 dB. The 8 IF unites of receiving element and the 48 IF unites' measurements are showed in Fig 12 and Fig13 respectively, it realizes a dual-conversion receiver with I/Q demodulator and their measurement results have good consistency whose amplitude error are smaller than 0.5 dB. As is shown in Fig 14 their orthogonal error are smaller  $5^\circ$  in the  $\pm 200\text{MHz}$  bandwidth. From Fig. 6 to Fig. 14 the gain of the receiving element can be realized at 80 dB which has a 4.1 dB noise figure. The nominal gain and noise figure of the receivers are  $\sim 80$  dB and  $\sim 4.2$  dB respectively. In order to equalize the gain between channels, the gain of each IF module can be adjusted by a variable attenuator.

The mmW front end converts the mmW signal into lower frequency signal, which will be then demodulated into I/Q outputs by the IF module. The first stage operates in single side band (SSB) mode for image rejection purpose, while the second stage operates in double side band (DSB) mode. DSB is

used because the analytic signals is free from frequency image. Thus, it do not needs image-reject filter and results in lower receiver volume. The configuration of the receiver array is demonstrated in Fig. 3. Since the dimension of the receiver cross section is  $20\text{mm} \times 20\text{mm}$  and is larger than  $1.46\lambda = 12.9\text{mm}$ , an interleaving method is adopted in the vertical arm.

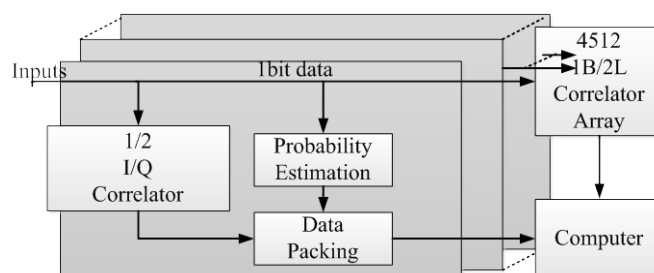


Fig.16. Block diagram of the DSP subsystem

### 3.3 Digital Signal Processing Subsystem

The I/Q outputs of the receivers are digitized and the complex correlations between signals are calculated in the DSP subsystem. 1bit/2level (1B/2L) correlators [22] are used for simplicity, because of the 2676 correlators of DSP subsystem. The correlation coefficient of the input signals is given by 1B/2L correlator only gives, and the power of the input signals are measured to denormalize the coefficients into visibility function samples.

The block diagram of the DSP subsystem is illustrated in Fig. 16. For BHU-2D-U, a typical integration time is about 0.1s~5s, which corresponds to a 31-bit counter in the 1B/2L correlator[23]. Finally, after collecting the measurements, he visibility function samples could be calculated by the computer. By calculating the IFT of the visibility function samples, a brightness temperature image could be obtained in the computer.

## 4 Experimental Result

As is shown in Fig. 17, the components of BHU-2D-U have been developed and assembled at present,. In order to validate the design, imaging experiments on a point source and a person are conducted who take a telephone and a knife respectively.

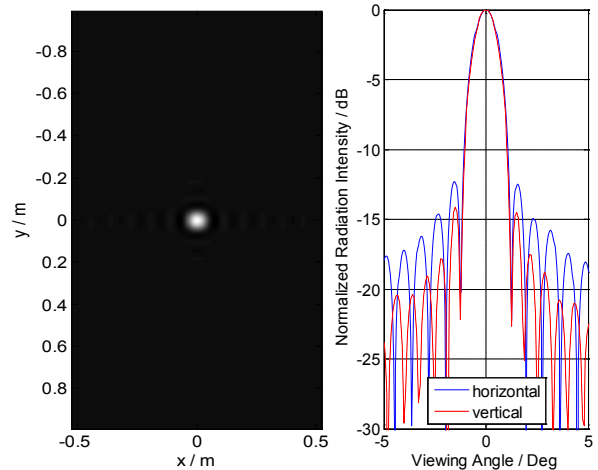
### 4.1 Imaging Result of a Point Source

The point source is located in front of the instrument and the distance between them is about 3m. The image of the point source can be interpreted as the point spread function (PSF) of the system, because

the solid angle subtended by the point source is smaller than the imaging resolution. The measurement result is showed in Fig. 18(a). Hanning window is applied before image reconstruction to reduce the influence of the side lobe. Fig. 18(b) shows the cross-section of the PSF. It is showed that the angular resolution is about  $1.3^\circ \times 1.3^\circ$ , which is consistent with the design specification.

**4.2 Imaging Result of a Person**

Imaging experiment on a person who hold a mobile telephone and a knife respectively is carried out. In order to form a uniform cold background, a metal plane with  $45^\circ$  incline to the ground is fixed. The plane can reflect the spontaneous radiation from the sky and form a uniform cold background. The integration time in the experiment is set to 0.5s. The results are shown in Fig. 20. The pictures shown on the left is captured by a camera and the corresponding imaging results are on the right. Fig. 19(a) shows that the image obtained by BHU-2D-U matches the picture taken by the camera very well.



(a) PSF of BHU-2D-U (b) Cross-section of the PSF

Fig.18. PSF of BHU-2D-U

A mobile telephone is held and it can be showed clearly from the mmW image. It also can be seen that the brightness temperature distribution of a person is not uniform. It might be caused by the reflection of the environment. In Fig. 19(b), a knife is held in the person's hand and it can be recognized clearly from the mmW image, although it is concealed under his shirt.



Fig.17. Photograph of the BHU-2D-U



(a) Imaging result of a person holding a mobile telephone



(b) Imaging result of a person with a concealed knife

Fig.19. Imaging results of a person

## 5 Conclusion

In order to meet the requirements of the applications in whole human body scan at the security check point. The BHU-2D-U is developed by Beihang University which is an improved model of the passive mmW imager BHU-2D. A U-shaped antenna array is used, and the receiver is designed and measured and some specification of the components are also modified. Initial results of imaging experiments show that BHU-2D-U is capable of detecting concealed weapons.

### References:

- [1] Liu S, Jin H. X-ray security inspection technology[J]. Journal of Security University: Science and Technology, 2008, Vol.58, No.4, pp.78-80.
- [2] D. A. Wikner, "Progress in millimeter-wave imaging," in Proc. SPIE, vol. 7936, Feb. 10, 2011, 79360D.
- [3] V. G. Kolinko, S. Lin, A. Shek, W. Manning, C. Martin, M. Hall, O. Kirsten, J. Moore and D. A. Wikner, "A passive millimeter-wave imaging system for concealed weapons and explosives detection," in Proc. SPIE, vol. 5781, May. 19, 2005, pp.85-92.
- [4] J. A. Lovberg, C. Martin and V. G. Kolinko, "Video-Rate Passive Millimeter-Wave Imaging

- Using Phased Arrays," in Proc. MWSYM, Honolulu, HI, Jun. 3-8, 2007, pp.1689-1692.
- [5] Bao-Hua Yang, Ghulam Mehdi, Anyong Hu, etc., "The Round-ended Design and Measurement of All Symmetric Edge-coupled Bandpass Filter", Progress In Electromagnetics Research C, Vol. 136, 2013, pp:17-27..
- [6] T. D. Williams and N. M. Vaidya, "A Compact, Low-Cost, Passive MMW Security Scanner," in Proc. SPIE, vol. 5789, May. 19, 2005, pp.109-116.
- [7] D. Notel, J. Huck, S. Neubert, S. Wirtz and A. Tessmann, "A compact mmW imaging radiometer for concealed weapon detection," in Proc. IRMMW-THz, Cardiff, Sep. 2-9, 2007, pp. 269-270.
- [8] W. Kim, N. Moon, Y. Chang, M. Lee, S. Jung, J. Choi, J. Jung and Y. Kim, "System design of focal plane array based millimeter-wave imaging radiometer for concealed weapon detection," in Proc. IGARSS, Vancouver, BC, Jul. 24-29, 2011, pp.2258-2261.
- [9] H. Lee, D. Lee, S. Yeom, J. Son, V. P. Guschin and S. Kim, "Passive millimeter wave imaging and analysis for concealed object detection," in Proc. ICMiA, Macao, Oct. 24-26, 2011, pp.98-101.
- [10] A. Doghri, A. Ghiotto, T. Djeraji and K. Wu, "Early demonstration of a passive millimeter-wave imaging system using substrate integrated waveguide technology," in Proc. MMS, Hammamet, Sep. 8-10, 2011, pp.215-218.
- [11] N. A. Salmon, J. Beale, A. Beard, M. Dean, S. Hayward, P. Hickling, S. T. Chiw, H. Ghafouri-Shiraz, P. Hall, R. Macpherson, R. Lewis, A. H. Lettington and D. Dunn, "An all electronic passive millimetre wave imaging system," in Proc. SPIE, vol. 5789, May. 19, 2005, pp.11-15.
- [12] N. A. Salmon, J. Beale and S. Hayward, "Compact and light-weight digital beam-forming passive millimeter imagers," in Proc. SPIE, vol. 7117, Oct. 2, 2008, 711709.
- [13] N. A. Salmon, R. Macpherson, A. Harvey, P. Hall, S. Hayward, P. Wilkinson and C. Taylor, "First video rate imagery from a 32-channel 22-GHz aperture synthesis passive millimetre wave imager," in Proc. SPIE, vol. 8188, Oct. 6, 2011, 818805.
- [14] N. A. Salmon, P. N. Wilkinson, C. T. Taylor and M. Benyazzar, "Minimising the costs of next generation aperture synthesis passive millimetre wave imagers," in Proc. SPIE, vol. 8188, Oct. 6, 2011, 818808.

- [15] Yong Xue, Jungang Miao, Guolong Wan, Anyong Hu, Feng Zhao, "Prototype development of an 8mm band 2-Dimensional aperture synthesis radiometer", 2008 International GeoScience and Remote Sensing symposium, Boston.
- [16] Hu Anyong and Miao Jungang, "Prototype development of an 8mm-band two dimensional interferometer synthetic aperture radiometer," in Proc.IEEE IWISA 2009
- [17] C. Zheng, X. Yao, A. Hu, and J. Miao, "A passive millimeter-wave imager used for concealed weapon detection," Progress In Electromagnetics Research B, pp. 379-397, 2013.
- [18] C. Zheng, X. Yao, A. Hu, and J. Miao, "Statistical power measurement unit for an 8MM-band two dimensional synthetic aperture interferometric radiometer BHU-2D," Progress In Electromagnetics Research M, vol. 27, pp. 119-128, 2012.
- [19] I. Corbella, A. Camps, F. Torres and J. Bara, "Analysis of Noise-Injection Networks for interferometric-radiometer calibration," IEEE Trans. Geosci. Remote Sens., vol. 48, no. 4, pp. 545-552, Apr. 2000.
- [20] A. Camps, "Application of interferometric radiometry to earth observation," Ph.D. dissertation, Polytechnic University of Catalonia, Spain, 1996, ch. 3
- [21] C. S. Ruf, "Digital correlators for synthetic aperture interferometric radiometry," IEEE Trans. Geosci. Remote Sens., vol. 33, no. 5, pp. 1222-1229, Sep. 1995.
- [22] I. Corbella, F. Torres, A. Camps, A. Colliander, M. Martín-Neira, S. Ribo, K. Rautiainen, N. Duffo and M. Vall-Ilossera, "MIRAS end-to-end calibration: application to SMOS L1 processor," IEEE Trans. Geosci. Remote Sens., vol. 43, no. 5, pp. 1126-1134, May. 2005.
- [23] C. Zheng, X. Yao, A. Hu, and J. Miao, "Closed form calibration of 1bit/2level correlator used for synthetic aperture interferometric radiometer," Progress In Electromagnetics Research M, vol. 29, pp. 193-205, 2013.